nature communications

Article

https://doi.org/10.1038/s41467-024-53549-y

Solvent-adaptive hydrogels with lamellar confinement cellular structure for programmable multimodal locomotion

Received: 17 June 2024

Accepted: 16 October 2024

Xin Yao[1], Hong Chen[1], Haili Qin[1], Qi-Hang Wu[1], Huai-Ping Cong[1] & Shu-Hong Yu[2,3]

Biological organisms can perform flexible and controllable multimodal motion under external stimuli owing to the hierarchical assembly of anisotropic structures across multiple length scales. However, artificial soft actuators exhibit the limited response speed, deformation programmability and movement capability especially in harsh environments because of insufficient anisotropic hierarchy and precision in structural design. Here, we report a programmed assembly directed confinement polymerization method for the fabrication of environmentally tolerant and fast responsive hydrogels with lamellar assembly-confined cellular structure interpenetrated with highly aligned nanopillars by the directional freezing-assisted polymerization in the predesigned anisotropic laminar scaffold. The obtained hydrogel exhibits ultrafast responsiveness and anisotropic deformation exposed to temperature/light/solvent stimulation, maintaining highly consistent responsive deformation capability in all-polarity solvents over 100 days of soaking. Moreover, the hydrogels implement photoactive programmable multi-gait locomotion whose amplitude and directionality are precisely regulated by the intrinsic structure, including controlled crawling and rotation in water and non-polar solvents, and 3D self-propulsion floating and swimming in polar solvents. Thus, this hydrogel with hierarchically ordered structure and dexterous locomotion may be suitable for flexible intelligent actuators serving in harsh solvent environments.

The living organisms with elaborate hierarchical architecture that perform fascinating stimuli-responsive morphing behaviors have long been a source of inspiration for the design and manufacture of soft actuators[1–3]. Hydrogels with a crosslinked polymer network in water are of growing attention as soft smart actuation materials in the fields of moving robotics[4,5], haptic device[6] and biomedical engineering[7], owing to their biological tissue similarity, good flexibility and high degree of freedom triggered by ambient stimuli. Based on the osmotic pressure-driven de-swelling/swelling[8], isotropic contraction/expansion is generally performed for the hydrogels with homogeneous network structure under the global stimulation[9,10]. Furthermore, conventional hydrogels usually suffer from weak environmental adaptability and stability when exposed to a liquid arising from

---

[1] Anhui Province Engineering Research Center of Flexible and Intelligent Materials, School of Chemistry and Chemical Engineering, Hefei University of Technology, Hefei, P. R. China. [2] Institute of Innovative Materials, Department of Chemistry, College of Science, Southern University of Science and Technology, Shenzhen, P. R. China. [3] New Cornerstone Science Laboratory, Division of Nanomaterials & Chemistry, Hefei National Research Center for Physical Sciences at the Microscale, Department of Chemistry, University of Science and Technology of China, Hefei, P. R. China. e-mail: hpcong@hfut.edu.cn; yush@sustech.edu.cn

the mutually exclusive mechanism of loose crosslinking of polymer network for fast response to stimuli[11].

Inspired by high arrangement of collagen fibers enabling the skeletal muscles to implement anisotropic movements under heavy loading cycles[12], great efforts have been devoted to constructing the intricate yet programmable anisotropic architectures through the introduction of highly aligned nanounits into polymeric hydrogel network by applying electric/magnetic/acoustic fields or shear force to orient nanomaterials before or during the gelation process[13–16]. However, because the hierarchy and precision of the assembly structure in the reported anisotropic hydrogels are far lagging behind that of natural biological tissues, they behave the limited three-dimensional (3D) configurational changes and bionic movements[17,18]. Especially, their actuating speeds are limited to several minutes by sluggish deswelling and swelling processes determined by the diffusion of water molecules upon exposure to stimuli[9,19–21].

Cellular architectures with high mechanical robustness having aligned open porous interconnected network to provide fast liquid transport channels may resolve the conflict between fast actuating speed and long-term actuation stability[22–24]. Introducing cellular network structure into stimuli-responsive hydrogels has shown effectiveness in improving responsive speed and environmental tolerance owing to strong capillary effect, large water diffusion coefficient, low liquid flow resistance and mechanical stability as well as facile wet-shaping fabrication technique[25,26]. Unfortunately, only isotropic deformations are shown for the reported cellular hydrogels under stimuli as their thickness is reduced to micrometer to millimeter scales along the pore direction when serving as the actuators[26–28]. Therefore, it is highly desired to exert hierarchical anisotropy and robust constituents into cellular structure across multiple length scales if anisotropic hydrogel actuators are advanced with simultaneously rapid actuation speed and high environmental adaptability, but remains challenging.

Here, we demonstrate a programmed assembly directed confinement polymerization strategy for the fabrication of environmentally tolerant and multi-responsive hydrogels with lamellar assembly-confined cellular structure interpenetrated with highly aligned nanopillars by the directional freezing-assisted polymerization of poly(N-isopropylacrylamide) (PNIPAM) in the predesigned anisotropic laminar silver nanowire (AgNW)/sodium alginate (SA) aerogel (ASAA) scaffold. Benefiting from hierarchically anisotropic and robust structure with low-tortuosity mass transport channels, the obtained hydrogel exhibits fast anisotropic stimuli-responsive deformation in harsh environments, outperforming the reported thermally active hydrogel actuators, and high long-term stability with nearly unchanged responsive rates in all polarity solvents over 100 days. Furthermore, photoactive programmable multi-gait motions, including steered crawling and rotation in water and nonpolar solvents, and 3D self-propulsion floating and swimming in polar solvents are realized, whose magnitude and directionality are precisely pre-coded in inherent structural orientation of the hydrogel actuator. This work provides useful insights into the design and construction of flexible smart actuators for steady application in extreme environments.

Results

Fabrication of hierarchically anisotropic structure

A lamellar assembly confined-cellular architecture design strategy was developed to fabricate a fast responsive and environmentally tolerant hydrogel integrated with hierarchically anisotropic structure by a consecutive freezing-induced assembly and freezing-assisted confinement polymerization process. As illustrated in Fig. 1a, the mixture of 25 mg mL^{-1} of AgNWs (diameter: 60–100 nm, length: ~15 μm) and 20 mg mL^{-1} of SA was first dropped onto a silicone mold placing in a self-made bidirectional freezing device (Supplementary Figs. 1 and 2). After the bidirectional freezing assembly and the subsequent freeze-drying, the ASAA scaffold was obtained and further ionically crosslinked for mechanical enhancement by immersing in ethanol solution of $CaCl_2$ (20 mg mL^{-1}) for 10 min followed by solvent exchange with deionized water. The ASAA exhibited a typical lamellar structure consisting of 2 μm-thick lamellae with the spacing of ~50 μm (Fig. 2a, b). High-magnification SEM image captured that abundant of highly oriented AgNW/SA nanopillars were interpenetrated between the adjacent lamellae (Fig. 2c). Based on the inherent 1D geometric anisotropy of hydrophilic AgNWs, the nanopillar configuration among the lamellae in ASAA scaffold was regulated by the content of AgNWs[29]. At a low content of 10 mg mL^{-1}, the nanounits tended to be repelled into the gap by the growing ice branches, forming a layered microstructure parallel to the direction of freezing front movement with the sporadically-distributed nanopillars among 30 μm-spaced lamellae (A_{10}SAA) (Supplementary Fig. 3a–c). As the AgNW content increasing to 25 mg mL^{-1}, the enhanced interactions between the AgNWs and SA restricted the movement of nanofillers and strengthened linear arrangement of the AgNWs. A small fraction of AgNWs and SA was entrapped within the ice crystals by tip-splitting and subsequent healing, leading to the formation of the nanopillars between adjacent layers. At a 45 mg mL^{-1} of AgNW, the spacing between lamellae was increased to ~70 μm, and the microwalls were formed among the adjacent layers, leading to the decrease in structural anisotropy (A_{45}SAA) (Supplementary Fig. 3d–f).

Subsequently, the polymerizable precursor solution containing N-isopropylacrylamide (NIPAM) and carbon nanotubes (CNTs) was filled into the predesigned ASAA matrix and unidirectionally frozen in the direction parallel to the ASAA lamellae by an ice templating assembly technique at −30 °C (Fig. 1a). Noted that to prevent the polymerization of the precursor solution before directional freezing assembly, the temperature of above mixture was controlled at ~5 °C in the filling process. After two-stage confinement polymerization at −18 °C for 18 h and 25 °C for 5 h, a PNIPAM/CNT hydrogel network was confined within the ASAA scaffold. Thus, a hierarchically anisotropic hydrogel was finally fabricated, denoted as ASPC hydrogel. The obtained hydrogel inherited the laminated architecture from the ASAA with the lamellar spacing slightly expanded to ~60 μm (Fig. 2d and Supplementary Fig. 4). Enlarged top-view SEM image showed that 3D interconnected open porous honeycomb network with the pore size of 10–25 μm was homogeneously distributed within layered framework of the ASPC hydrogel (Fig. 2e). Parallel to the growth direction of ice crystals, a secondary interconnected lamellar network with low tortuosity having the spacing of 6–10 μm was uniformly arranged in the neighboring AgNW/SA layers (Fig. 2f, g). Uniform distributions of Ag, C, O and N elements in elemental mappings confirmed the incorporation of PNIPAM/CNT gel within the ASAA scaffold (Supplementary Fig. 5). Similarly, the A_{10}SPC and A_{45}SPC hydrogels prepared by the assembly of PNIPAM/CNT network within A_{10}SAA and A_{45}SAA scaffolds showed cellular network structure with different pore sizes confined in the layered framework (Supplementary Fig. 6a–f). Another control hydrogel by the polymerization of PNIPAM/CNT network in the ASAA framework displayed a closed cell network, defined as the ASAA-PC (Supplementary Fig. 6g–i).

X-ray microcomputed tomography (micro-CT) was further utilized for nondestructive visualization of full image of the ASPC based on X-ray sensitive to the materials density[30]. An anisotropic lamellar structure aligned on the macroscale was reconstructed (Fig. 2h). Cross-sectional images stemming from 3D stereogram showed aligned pores within the network, wherein abundant nanopillars perpendicular to the thin layer were observed in *xy* plane of the ASPC (Fig. 2i and Supplementary Fig. 7). SEM images, high-angle annular dark field scanning transmission electron microscope (HAADF-STEM) images and elemental mappings were conducted on ultrathin slices of the hydrogel parallel to the lamellae. Abundant Ag species were demonstrated at the cross sections of the slice, which inherited from the cut-off tips of

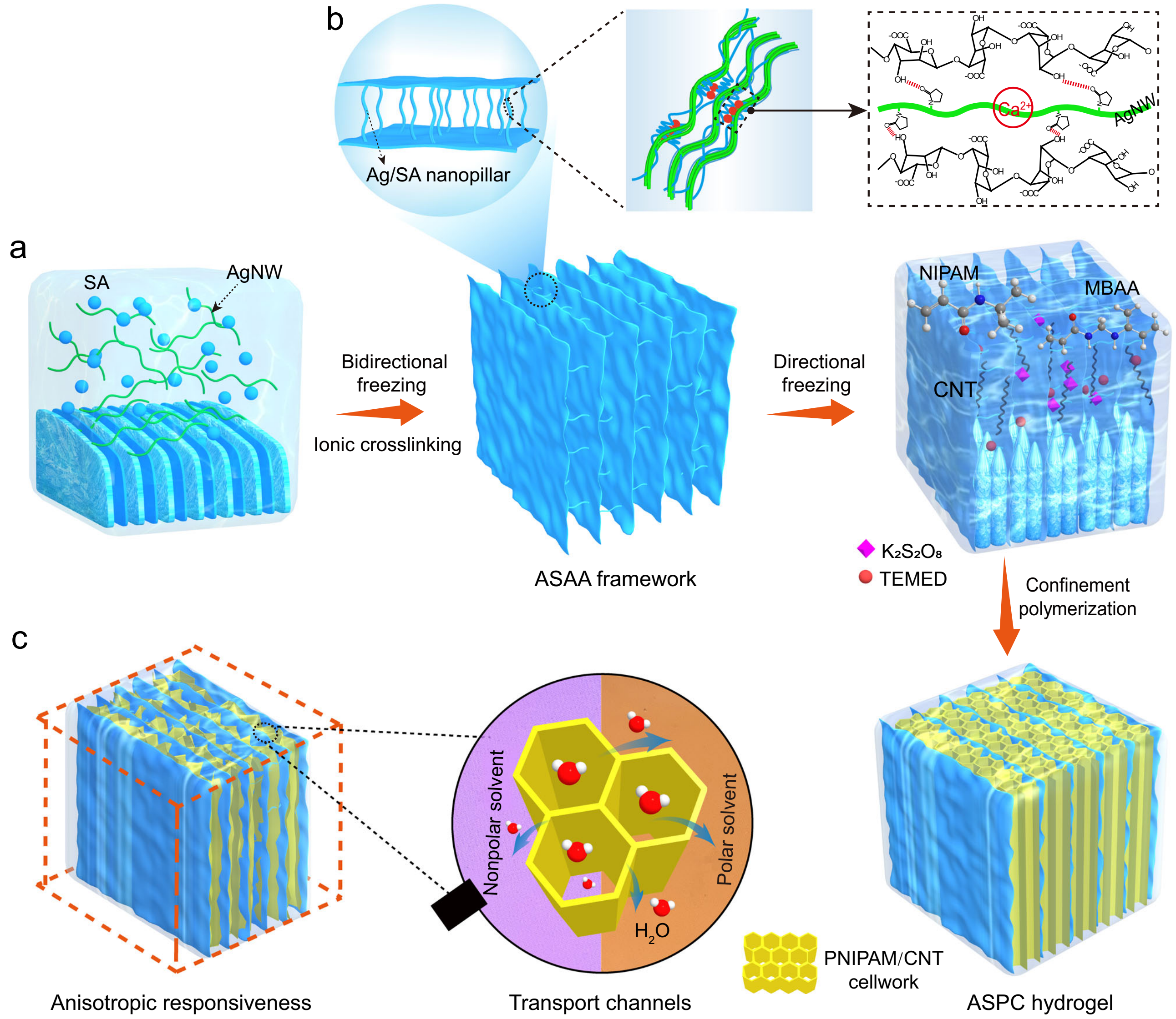

Fig. 1 | Design and fabrication of ASPC hydrogel. a Schematic illustration of the fabrication of the ASPC hydrogel from ASAA framework by the predesigned lamella-confined and freezing assembly-assisted polymerization process. A layered framework was firstly prepared by bidirectional freezing of the dispersion of AgNWs and SA and crosslinking by calcium ions. Then, the polymerizable solution of NIPAM, MBA, $K_2S_2O_8$ and CNTs was backfilled into the ASAA scaffold and directionally frozen parallel to the lamella with the addition of TEMED. After the cryopolymerization and room-temperature polymerization, the ASPC hydrogel with lamellar assembly-confined cellular structure was finally fabricated. **b** Schematic diagram illustrated the formation of highly-aligned AgNW/SA nanopillars interpenetrated between the adjacent lamellae in ASAA scaffold. **c** Schematic illustration of anisotropically responsive deformation of the ASPC hydrogel in different solvent environments with the help of accelerated transportation of water molecules through the low-tortuosity open porous channels.

AgNW/SA nanopillars interpenetrated among the ASAA lamellae (Supplementary Figs. 8 and 9). In Raman scattering mappings, no obvious Raman signal was observed between the AgNW/SA lamellae of the A_{10}SPC hydrogel at a low AgNW content (Supplementary Fig. 10a, b). With increasing the AgNW content, the enhanced Raman signal with a pillar configuration resulting from surface plasmon resonance of AgNWs was recorded in-between the lamellae of the ASPC hydrogel (Fig. 2j–l)[31]. Comparatively, a microwall-shaped image with the greatly-enhanced Raman intensity was scanned between the A_{45}SPC lamellae at a high AgNW content (Supplementary Figs. 10c, d). These results indicated that the ASPC held the architecture of AgNW/SA nanopillars interpenetrated across the PNIPAM/CNT network between the AgNW/SA lamellae, which not only ensured the material integrity, but also stored more elastic energy for elastic deformation and recovery of the hydrogel network.

Distinctive from traditional cellular structure, a four-level anisotropic hierarchy was built in the ASPC hydrogel by the predesigned matrix-directed and space-confined polymerization strategy: the nanosized AgNWs were assembled into anisotropic AgNW/SA lamellae (first level); the directionally-frozen assembled PNIPAM/CNT compartmental units (second level) were then interconnected to form anisotropic honeycomb network, which was confined within the lamellar framework with the AgNW/SA nanopillars perpendicularly interpenetrated at tens of micrometers (third level) (Fig. 1b); following with long-range interlamination of AgNW/SA lamellae by PNIPAM/CNT cellular network, a macroscopic anisotropic assembly with fast transport channels was finally created (fourth level), showing great potentials in anisotropic responsive deformation (Fig. 1c).

Anisotropic deformations in all solvents

Owing to highly anisotropic lamella confinement honeycomb architecture, the ASPC hydrogel exhibited anisotropic deformation behaviors in liquids exposed to external stimuli, including temperature,

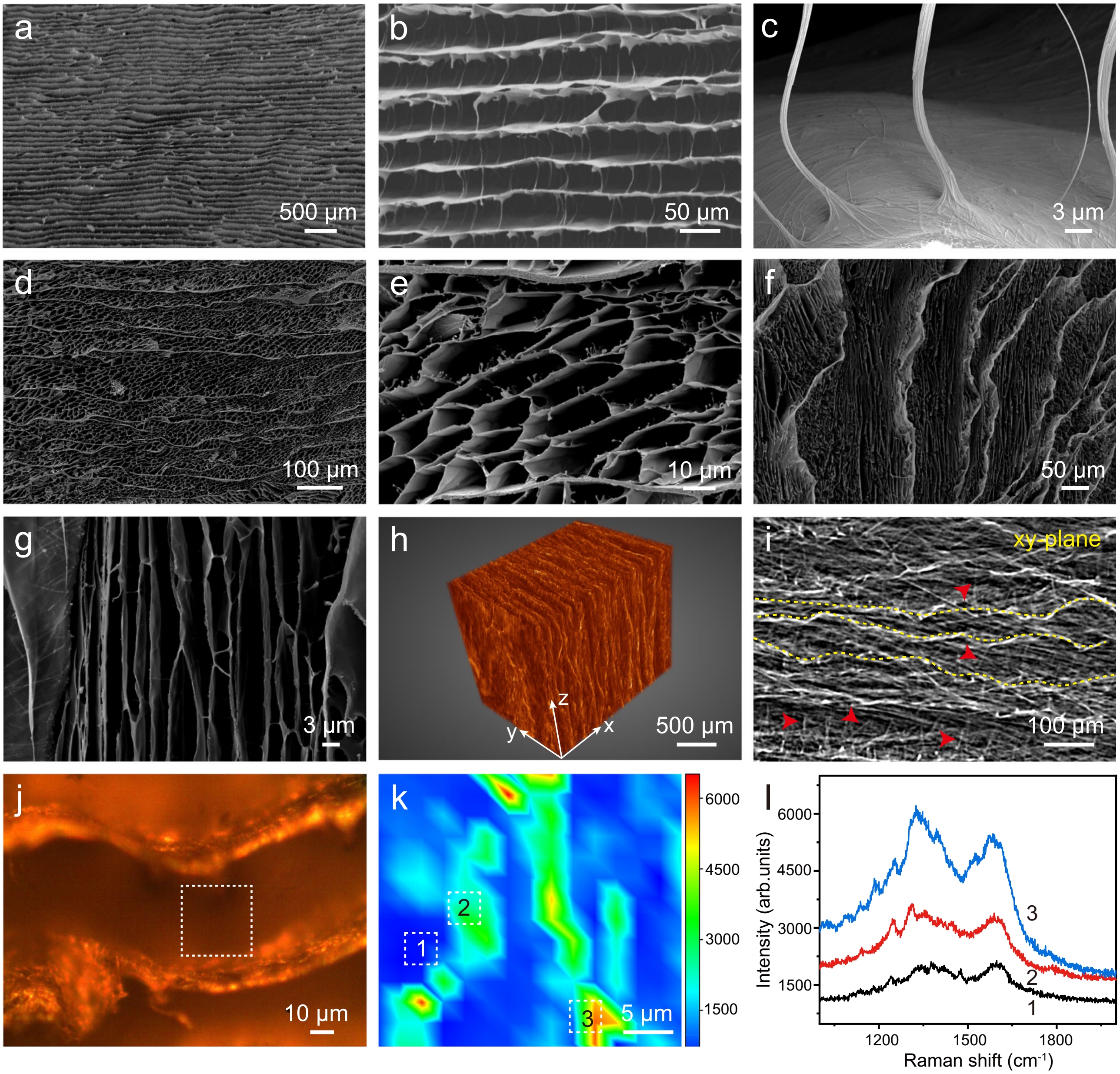

Fig. 2 | Structural characterization of ASPC hydrogel. a–c SEM images with different magnifications of the ASAA scaffold. **d–g** SEM images with different magnifications of the ASPC hydrogel: top view (**d**, **e**); side view (**f**, **g**). Micro-CT of the ASPC hydrogel (**h**) and its structure perpendicular to the AgNW/SA lamellae (**i**). The yellow dashed lines and red arrows represented the lamellae and AgNW/SA nanopillars, respectively. **j** Optical image showing lamellar structure of the ASPC hydrogel. **k** Raman scattering mapping of nanopillars between the lamellae of the ASPC squared in (**j**). **l** Raman spectra of three regions squared in (**k**).

light and solvent (Fig. 3a, Supplementary Movie 1). When dipped in a 45 °C water bath, that was higher than the LCST of PNIPAM, the ASPC hydrogel abruptly contracted by 41.6% perpendicular to the AgNW/SA lamellae within 1.1 s with the unchanged length in the orthogonal direction (Fig. 3b and Supplementary Fig. 11a). Once transferred into a water bath at 25 °C, the shrunk hydrogel immediately expanded to the original shape within 1.05 s. The average deformation and recovery rates were measured to be 1.97 mm s^{-1} and 2.06 mm s^{-1}, respectively, which were faster than the reported thermally actuating hydrogels[13,14,17,25,27,28]. Furthermore, no apparent fatigue was observed after 100 deformation-recovery cycles (Supplementary Fig. 11b). Such notable anisotropic deformation benefitted from reinforced-concrete ASAA with ordered layered structure, which resisted strain along the parallel direction and allowed transverse strain (Supplementary Fig. 12). When the temperature was switched, the PNIPAM/CNT network stretched like a muscle, generating an anisotropic extension in the ASPC hydrogel. Even when placed in 45 °C water for 100 h, the hydrogel recovered rapidly within 5 s of cooling (Supplementary Fig. 13). Furthermore, the influences of the temperature of unidirectional freezing and the content of crosslinker on the thermal responsiveness of ASPC hydrogels were explored (Supplementary Fig. 14). With the freezing temperature decreasing from −30 °C to −120 °C, the contraction ratio of the obtained hydrogels perpendicular to the lamella decreased from 42% to 13% in 1.1–1.9 s, while the recovery time of the shrunk gels increased from 1.1 s to 2.5 s (Supplementary Fig. 14a, b), indicating the sluggish transport of water and the limited shrinkage of the network by a denser network when decreasing the freezing temperature. Similarly, as the crosslinker content increased, the increased crosslinking density of the polymer chains led to a decrease in both the shrinkage and actuation rate of the hydrogel

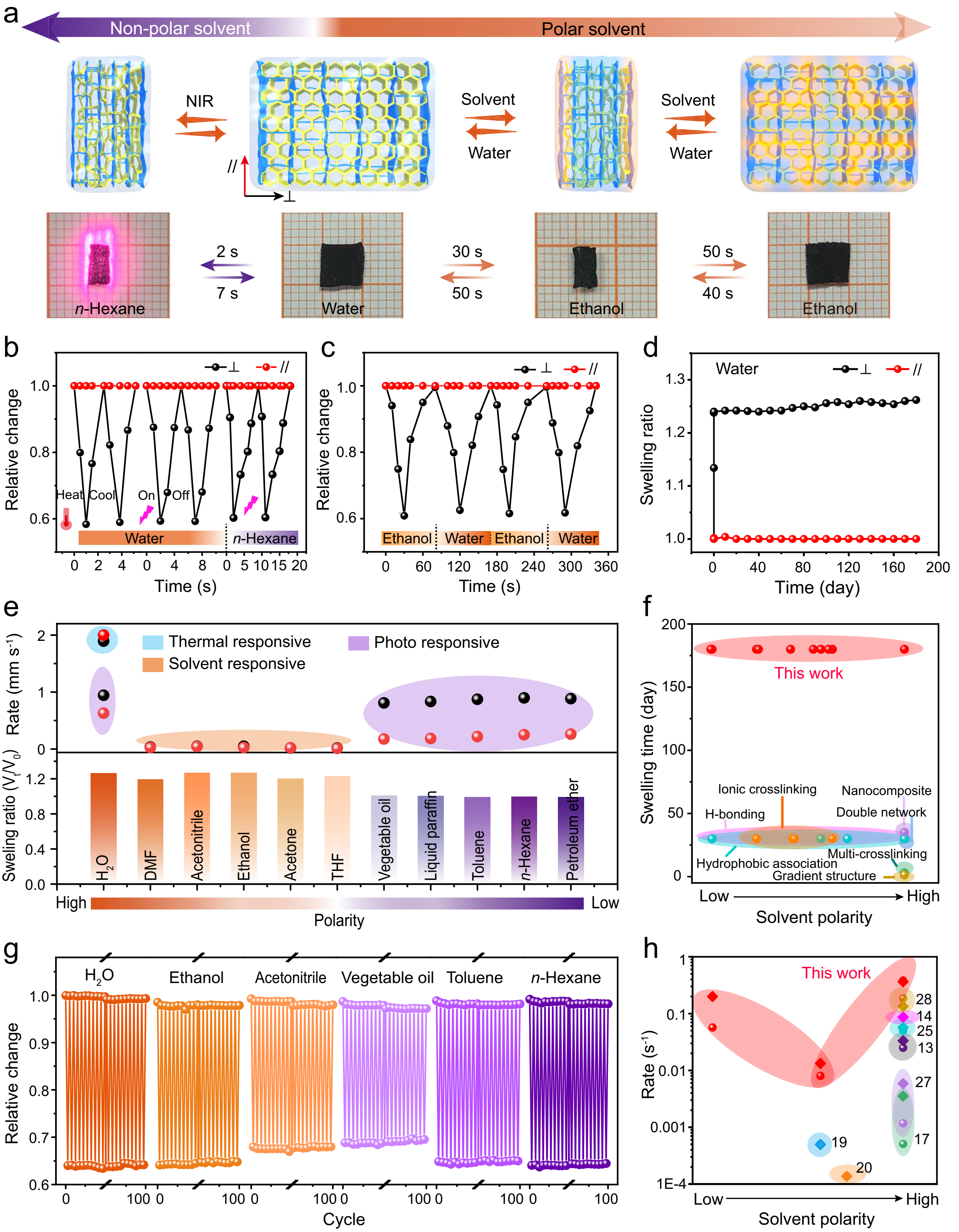

(Supplementary Fig. 14c, d). In contrast, the control $A_{10}SPC$ and $A_{45}SPC$ hydrogels showed decreased anisotropic deformations of 0.32 and 0.18 at slower deformation rates of 0.70 mm s^{-1} and 0.31 mm s^{-1}, respectively (Supplementary Fig. 15a, b). Because of lacking free channels for rapid water transportation, the recovery of the contracted ASAA-PC hydrogel was high up to 14 min (Supplementary Fig. 15c). The control hydrogel prepared by in-situ polymerization of PNIPAM and CNTs showed isotropic volume changes with a contraction of 58.1% after immersing in the hot water for 23 s and a sluggish recovery process up to 12 min in a water bath at 25 °C (Supplementary Fig. 15d).

Besides hot water, NIR irradiation triggered an anisotropic underwater deformation at a speed of 1.02 mm s^{-1} with a shrinkage of 40.7% perpendicular to the lamellae occurred in 2 s at a laser intensity of 1.5 W cm^{-2} arising from notable optical-to-mechanical energy

Fig. 3 | Anisotropic responsiveness in all-polarity solvents. **a** Schematic illustrations and corresponding optical images of anisotropic deformations of ASPC hydrogel in different solvents triggered by stimuli of light and solvent. **b** Relative changes of the ASPC hydrogel parallel and perpendicular to the AgNW/SA lamellae in water under thermal and NIR stimuli and in *n*-hexane under NIR stimuli. **c** Relative changes of the ASPC hydrogel parallel and perpendicular to the lamellae triggered by successive stimuli of ethanol and water. **d** Time-dependent swelling ratio of the ASPC hydrogel parallel and perpendicular to the lamellae in water over 180 days. **e** A summary of swelling ratio of ASPC hydrogel perpendicular to the lamellae in 11 solvents with different polarities after 180 days (low), and deformation (black sphere) and recovery rates (red sphere) of ASPC hydrogel after 100 days-swelling in different solvents under different stimuli (upper). **f** Ashby chart plotting anti-swelling stability versus solvent polarity of ASPC hydrogels compared with previously reported works. The pink, orange, purple, blue, cyan, green and yellow spheres represented hydrogels with H-bonding[45], ionic crosslinking[46], nanocomposite[47], double network[48], hydrophobic association[49], multi-crosslinking[50] and gradient structure[51] as anti-swelling mechanisms, respectively. **g** Cyclic stability of stimuli-responsive performance of ASPC hydrogels after swelling in different solvents for 100 days over 100 cycles. **h** Comparison of deformation (square) and recovery (sphere) rates (deformation/recovery ratio divided by the time) of ASPC hydrogel with previously reported works.

conversion capacity of the assembled AgNWs and CNTs in the ASPC hydrogel (Fig. 3b and Supplementary Fig. 16a). Once turning off the light, the hydrogel recovered to original shape at a rapid speed of 0.68 mm s^{-1} (within 3 s). Noted that the temperature of the control hydrogel without the CNTs only achieved 49.6 °C in 3 s, much lower than 72.5 °C of the ASPC hydrogel under the irradiation at 1.5 W cm^{-2} (Supplementary Fig. 16b), and shrunk by 22% perpendicular to the lamellae at a speed of 0.48 mm s^{-1} in 2 s (Supplementary Fig. 16c), suggesting important roles of CNTs in high actuation performance. With the merits of porous cellular network confined in lamellar structure providing highly free channels, the hydrogel afforded rapid and reversible photo-driven deformation in non-polar solvents including petroleum ether, *n*-hexane, toluene, liquid paraffin and vegetable oil, by quickly repelling/absorbing water through the channels under the action of siphon when on/off switching the light (Supplementary Fig. 17). After 100 deformation cycles, no obvious deterioration in responsiveness was detected. Even in high-viscosity liquid paraffin over 100 cycles, its deformation and recovery speeds decreased slightly from 0.94 to 0.86 mm s^{-1}, and 0.21 to 0.11 mm s^{-1}, respectively (Supplementary Fig. 18).

Impressively, the ASPC hydrogel exhibited cyclically anisotropic deformation when alternatively exposed to a polar solvent-cosolvent of PNIPAM, and water. For example, benefitting from the open low-tortuosity honeycomb network channels, ethanol quickly entered in the hydrogel network and competed with the amide groups on PNIPAM to form hydrogen bonds with water when the ASPC hydrogel was transferred from water to ethanol[32]. This destroyed the hydration structure between hydrophilic and hydrophobic regions, resulting in the shrinkage of PNIPAM network[33]. After soaking in ethanol for 30 s, the PNIPAM network reached a hydrophobic equilibrium in accompany with more ethanol molecules interacting with water molecules, and the hydrogel piece was shrunk by 39% along the direction vertical to the lamellae (Fig. 3a, c). With continually exchanging with ethanol molecules, PNIPAM network recovered under the synergy of hydrophobic interaction between isopropyl groups and hydrophobic domain of ethanol, and the increased number of hydrogen bonds between the amide bonds and hydroxyl of ethanol[33]. In the next 50 s, the shrunk gel was expanded to original shape with the molar ratio of ethanol increased from 0.15 to 0.30 (Supplementary Fig. 19a). Notably, such deformations were reversible with the decrease of ethanol content to 0.11 and 0.02 when soaking the above gel in water for 40 s and 90 s (Fig. 3c). The periodic exchange of ethanol and water was confirmed by reversible changes of intensity of υ(CH) peaks in Raman spectra at different deformation stages (Supplementary Fig. 19b)[32]. Under the cosolvency mechanism that controlled the interactions of solvent-water and solvent-hydrophilic/hydrophobic groups of PNIPAM chains, the hydrogel displayed a phase-separation network in the co-solvent environment with ethanol content ranging from 0.02 to 0.15, leading to anisotropic shrinkage[33,34]. With ethanol or water content increased, the conformation of polymer network got extended, leading to an appearance of shape recovery. Furthermore, the polar solvents of dimethyl formamide (DMF), acetonitrile, acetone and tetrahydrofuran (THF) also stimulated the ASPC hydrogel with anisotropic deformation in a reversible manner (Supplementary Fig. 20). Notably, stable and repeatable shape deformations without significant response hysteresis were observed by cycling a gel piece in different solvents and water for 50 cycles (Supplementary Fig. 21).

To evaluate long-term responsive stability of the ASPC hydrogel in liquids, the anti-swelling behavior was investigated by monitoring the changes in geometry over time. Swelling equilibrium was rapidly achieved within 3 s in water, due to capillary siphon effect and anisotropic structure, accompanied by an expansion of 25% perpendicular to the AgNW/SA lamellae and negligible changes in lamellar dimensions (Fig. 3d). For the subsequent 180 days of soaking in water, the morphology of the ASPC hydrogel almost kept unchanged. This strong water-resistant performance was attributed to anisotropic cellular PNIPAM/CNT network with free channels fixed into rigid, anisotropic ASAA framework, which significantly restrained the swelling of polymer network caused by osmotic pressure. Furthermore, the ASPC hydrogel displayed high adaptability in a variety of solvents with a wide polarity range (Low row in Fig. 3e). Soaking in polar solvents, the hydrogel first underwent anisotropic shrinkage-recovery deformation, and then expanded 18%–22% to achieve swelling equilibrium in the following 10–15 s (Supplementary Fig. 22a–e). Afterwards, it was stable over 180 days. Non-swollen performance was also observed during 180 days of soaking in non-polar solvents (Supplementary Fig. 22f). In contrast, the A_{10}SAA hydrogel exhibited a larger swelling ratio with an expansion of 37% perpendicular to the lamella after 10 days of immersion in water resulting from the layered structure with the fewer interconnections (Supplementary Fig. 23a). The weakened anisotropic swelling behavior of the A_{45}SPC was delivered with 20.4% and 3.2% of expansion perpendicular to the lamella and along the lamella, respectively, after soaking in water for 10 days (Supplementary Fig. 23b). The ASAA-PC hydrogel experienced the sluggish swelling equilibrium in accompany with a swelling ratio of 138% after 80 h (Supplementary Fig. 23c), resulting from slow water diffusion and poor mechanical robustness of the closed cell network.

Relying on strong adaptability in harsh liquid environments, the ASPC hydrogel maintained rapid, highly consistent photo/solvent-responsive capability without obvious deterioration in deformation and recovery rates even after soaking in various solvents over 100 days (Upper row in Fig. 3e and Supplementary Figs. 24 and 25), indicating its excellent long-term stability. After soaking in these solvents for 100 days, no apparent fatigue was observed over 100 actuating cycles stimulated by NIR or polar solvents (Fig. 3g). These results fully suggested the ASPC hydrogel having strong environmental tolerance and excellent stimuli-responsiveness in all solvents, outperforming the previously reported hydrogels (Fig. 3f, h), which confirmed its great potentials as flexible smart drives with anisotropic responses in extreme environments.

Programmable multimodal motions in water and nonpolar solvents

Hydrogel system has been widely developed in the design of bionic robotics owing to high mobility, high degree of freedom of deformation and high programmability[35]. Especially, the stimuli-responsive hydrogels containing active units can directly transform stimulation into macroscopic deformation and movements under the force/torque generated by physical/chemical reactions. With the help of an asymmetric shape design or a customized substrate, various locomotion gaits, including walking, crawling, rolling, jumping and swimming are achieved[36]. Benefitting from highly anisotropic hierarchical structure and cellular network with fast mass transport capability, the ASPC hydrogels could actualize rapid and stable anisotropic deformations in solvent environments, and further implement programmable locomotion exposed to periodic scanning of NIR light. The fundamental motion mechanism was that photo-induced contractile strain caused the friction competition between the head and tail of hydrogel, which mimicked the movements of the larvae relying on the synergistic effects between cyclic contraction and expansion of the body and asymmetric friction of the body and substrate[37]. When the NIR light scanned the gel under the water from right to left (Fig. 4a), a pair of contractile forces Fc_1 and Fc_2 rapidly generated on the head and tail by the contraction of polymer network with rising temperature, which sought to induce slip between the gel and substrate (polytetrafluoroethylene). The corresponding frictional resistances f_1 and f_2 were opposite to the directions of contraction forces. Note that the head slid slightly towards the tail at the beginning due to the speedy dehydration of the cell network. Arising from the hydrophilic-to-hydrophobic conversion of polymer chains, the friction coefficient μ_1 between the head and substrate increased correspondingly, leading to $\mu_1 > \mu_2$[38]. With persistent energy accumulation under continuous light exposure until the tail conquered static friction, where $Fc_2 > f_2$, and $Fc_1 = f_1$, the tail moved towards the stationary head. Once the light stimulating the tail, the shrunk head expanded rapidly with the help of low-tortuosity open cell network accelerating the transport of water, producing a pair of expansion forces Fe_1 and Fe_2. The recovery of hydrophilic polymer network at the head enabled $\mu_1 < \mu_2$, leading the head to slide forward ($Fe_1 > f_1$, and $Fe_2 = f_2$). Therefore, by cyclically scanning the hydrogel sheet, the telescoping peristaltic movements were generated following with continuous contraction and expansion deformations.

The influences of gel dimensions including length and width, and power intensity of NIR on the crawling velocity of ASPC hydrogel in water were explored. As for a short gel, the small energy accumulation and release of the deformable cell network resulted in a low crawling velocity. The crawling velocity increased accordingly to achieve a maximum velocity of 0.07 mm s^{-1} at the length of 7 mm (Supplementary Fig. 26a). Additionally, a gel with a long length also exhibited the decreased crawling velocity, which arose from the increased friction force that limited the movement of the gel. Upon increasing the width of the gel from 1 mm to 3 mm, the instability of the centroid under light caused by size effect was gradually overcome, resulting in an increase in crawling velocity (Supplementary Fig. 26b). But further increasing the width reduced the velocity because of the increased friction. Moreover, with increasing the intensity, the head of the gel could accumulate more energy in a short period of time, enabling the tail to overcome static friction and slid towards the head, ultimately leading to an increase in crawling velocity (Supplementary Fig. 26c).

Notably, the decisive force for the mobility, Fc, was always perpendicular to the AgNW/SA lamellas, due to deformable anisotropic cellular network confined to a rigid layered scaffold. Thus, the directionality of motion could be facilely regulated by altering inherent structural parameter α of the hydrogel sheet, which was defined as the orientation angle between the AgNW/SA lamellae and long axis direction of the cut sheet (Fig. 4b). At a fixed α except for 90°, a torque (τ) was generated by the component force of Fc in vertical direction ($F_{\perp} = Fc_2 \times \cos\alpha$), whereas the component in horizontal direction ($F_{//} = Fc_2 \times \sin\alpha$) drove for horizontal locomotion, enabling the hydrogel to achieve steered crawling in a controllable direction (Fig. 4c). The hydrogel sheet rotated anticlockwise while crawling when $0° < \alpha < 90°$ (defined as positive angle) and rotated clockwise while crawling when $90° < \alpha < 180°$ (Supplementary Fig. 27a). Due to the disappearance of the $F_{\perp}$ at $\alpha = 90°$, the rightward crawling was produced at a speed of 0.075 mm s^{-1} under cyclic light scanning from right to left. The cooperation of deformation and friction force was manifested by the discrete displacements of the head and tail at distinct periods of time (Fig. 4d). At $\alpha = 45°$ or 135°, a steered crawling in anticlockwise or clockwise direction was delivered with a total of 60° rotating angle and cumulative displacement of 4 mm over 13 scanning cycles (Fig. 4e, Supplementary Fig. 27b and Supplementary Movie 2).

The detailed relationship between the α and crawling trajectory (motion angle and horizontal displacement) of gel was illustrated (Fig. 4f). When the α increased from 0° to 90°, the $F_{//}$ was gradually enhanced, and therefore, the horizontal displacement of anticlockwise crawling was increased to 0.6 mm after a NIR scanning, which conformed to the sine function. On the other hand, at a larger α, it was faster to achieve energy accumulation threshold that conquered the friction force and triggered the tail to move forward, which produced the head with a smaller irradiated area (Supplementary Fig. 28). Thereby, a larger force arm L for the rotating motion was yielded that defined as the distance between the center of tail and the anchor (head) and was proportional to sinα. Meanwhile, the $F_{\perp}$ proportional to cosα was gradually decreased. Therefore, the torque that caused the tail to rotate around the anchor reached its maximum value at $\alpha = 45°$, enabling a largest motion angle of 6.5° per scanning cycle. At $90° < \alpha < 180°$, the gel sheet moved clockwise in similar movement magnitude. Noted that the crawling direction was always opposite to the scanning direction (defined as positive displacement). For example, when changing the scanning direction from left to right, the gel crawled leftwards at a speed of 0.073 mm s^{-1} at $\alpha = 90°$ (Supplementary Fig. 29a, b). Furthermore, it steered anticlockwise at $0° < \alpha < 90°$, and clockwise at $90° < \alpha < 180°$, respectively, while maintaining positive displacements (Supplementary Fig. 29c, d). To this end, both the direction and magnitude of crawling motion were preprogrammed into the internal structural parameter of hydrogel irrespective of external conditions like the irradiation direction and complex macroscopic geometry of gel (Fig. 4f and Supplementary Fig. 30).

In addition to the steerable crawling, the rotating motion with controllable direction could be realized by changing the scanning mode of NIR light (Supplementary Movie 3). When the light scanned the gel diagonally, the rotational contraction force F_R perpendicular to the lamellas generated in the irradiation area was decomposed along the diagonal (Fig. 4g). The component force perpendicular to the diagonal ($F_{R\perp}$) propelled the generation of a torque to rotate around the centroid, while the static friction force arising from the component force parallel to the diagonal ($F_{R//}$) prevented a shift along the light scanning path. With the energy accumulation, a rotation was generated. Specifically, for the hydrogel at $\alpha = 90°$, when exerting 26 scanning cycles from the upper left to lower right, it rotated clockwise around its center of gravity to 180° in an increment of about 7° per cycle (Fig. 4g). However, When the light was applied for 30 scanning cycles from the top right corner along the diagonal of the gel, it rotated anticlockwise around the centroid to 180°, with an average increase of about 6° for each cycle. (Supplementary Fig. 31). In addition, it was measured that the optimal length (l) and width (w) of the gel for the rotation were 7 mm and 3.5 mm, respectively (Supplementary Fig. 32).

When the light scanned the gel diagonally from the upper left, as the driving force of the rotation, $F_{R\perp}$, was expressed by the equation: $F_{R\perp} = F_R \times \cos(\alpha + \varphi)$, where φ was defined as the angle between the diagonal and long axis of the gel (Supplementary Fig. 33a). When the light scanned the gel diagonally from the top right corner, $F_{R\perp}$ was expressed by the equation: $F_{R\perp} = F_R \times \cos(\alpha - \varphi)$ (Supplementary Fig. 33b). Based on $l = 7$ mm and $w = 3.5$ mm, the φ was calculated to be ~27°. When the F_R was generated along the diagonal, where $\alpha + \varphi = 90°$ or $\alpha - \varphi = 90°$, the gel could not rotate as the $F_{R\perp}$ was equal to zero.

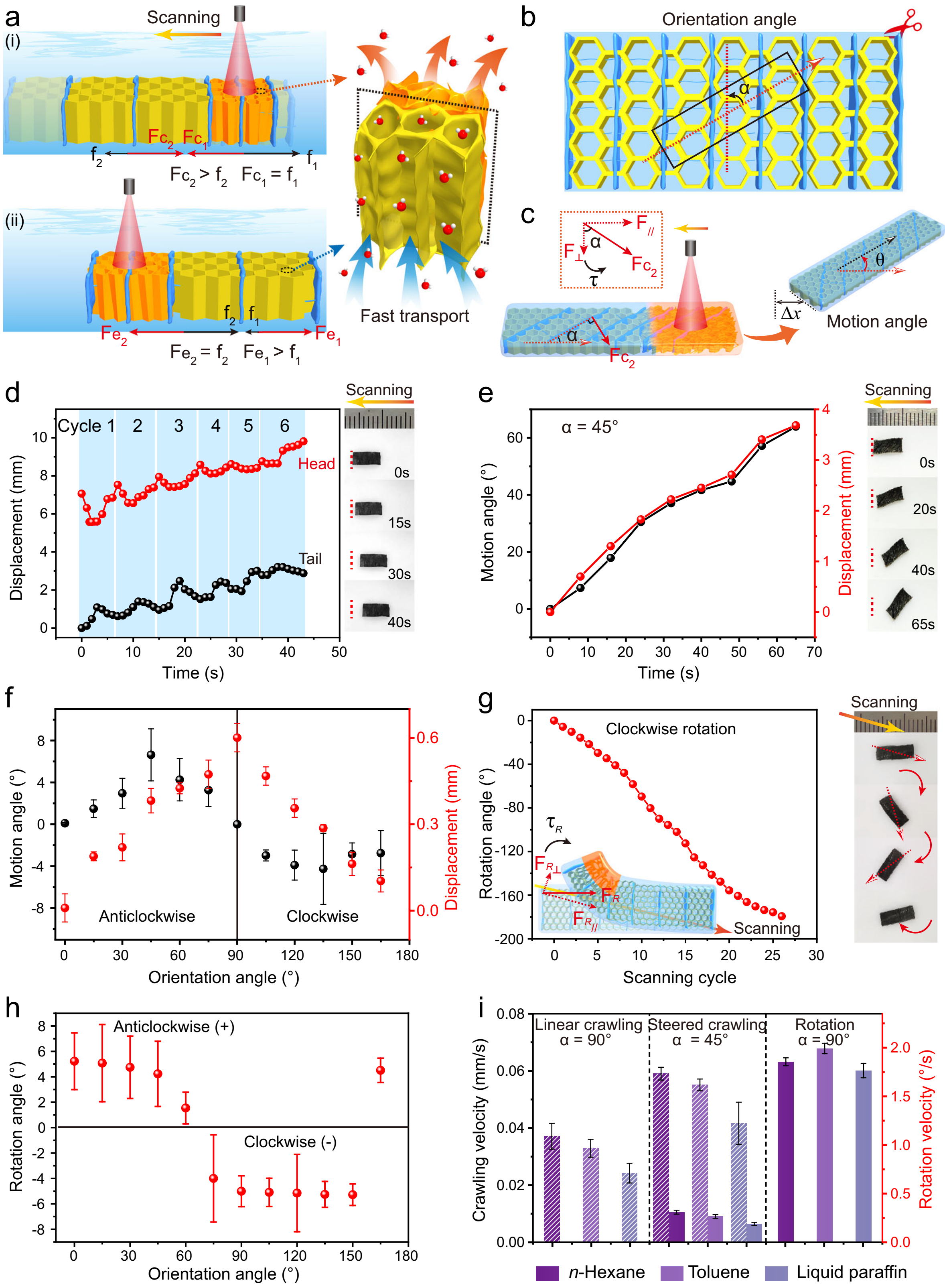

Thus, the critical value of α was ~63° for the light scanning from the upper left and ~117° for the light scanning from the upper right. Taking light scanning gel diagonally from the upper left corner as an example, at 0° ≤ α < 63° and 153° < α < 180°, the gel rotated anticlockwise and the rotation angle gradually decreased with the increase of α. Contrarily, the clockwise rotation was occurred when 63° < α ≤ 153°. The experimental results were highly consistent with the above analyses where a critical α of 60° was measured, indicating good motion controllability (Fig. 4h).

Furthermore, the ASPC hydrogel exhibited excellent adaptability including steerable crawling and rotation in non-polar solvents such as petroleum ether, *n*-hexane, toluene, paraffin and vegetable oil. Notably, the gel behaved phototropic motion in non-polar solvents (Supplementary Movie 4). Taking *n*-hexane as an example, because the

Fig. 4 | Steerable crawling and rotation in water and non-polar solvents. **a** Schematic illustration of the photodriven crawling of hydrogel sheet in water. During the scanning, the contraction forces (Fc_1 and Fc_2) or expansion forces (Fe_1 and Fe_2) competing with frictional forces (f_1 and f_2) enabled the gel to move opposite to the light. Schematic on the right showed open and low-tortuosity cell network as fast mass transfer channels to accelerate the release (i) and absorption (ii) of water. **b** Schematics of orientation angle (α) defined as the angle between the lamellae and long axis of the gel. **c** Motion trajectory and force analysis showing the controllable crawling dictated by regulating the α. The contraction force Fc acting on the tail was decomposed into a component force $F_{//}$ to drive horizontal movement Δx and a vertical component force $F_{\perp}$ to drive the motion angle θ. A torque τ was generated at the tail. **d** Optical images of the gel (α = 90°) and time-variant displacements of the head and tail under cyclic scanning from right to left. **e** Optical images, time-variant displacements and motion angles of the gel (α = 45°) under cyclic scanning. **f** Motion angle (black sphere) and displacement (red sphere) were summarized as a function of α (negative signs indicated clockwise movements). **g** Schematics, optical images and rotated angle of the gel (α = 90°) under cyclic scanning along the diagonal direction. The component force $F_{R\perp}$ of contraction force F_R perpendicular to the diagonal generated a torque τ_R to actuate rotational dynamics. The red dashed arrows and red solid arrows indicated the scanning and rotation direction, respectively. **h** Rotation angle was summarized as a function of α. **i**, Summary of linear crawling, steered crawling and rotation of hydrogel with different α in non-polar solvents, such as *n*-hexene, toluene and paraffin. Striped and solid columns represented crawling velocity and rotation velocity, respectively. Data in (**f**), (**h**), and (**i**) are presented as mean values ± SD ($n = 3$).

water released by the polymer network of the irradiated area formed a lubrication layer between the gel and substrate, the friction was reduced correspondingly[39]. As a result, when light irradiated on the head, the contracted head moved towards the tail under the effect of $Fc_1 > f_1$, and $Fc_2 = f_2$. Since the light removed away the head and irradiated on the tail, the synergy of the expansion of the head and shrinkage of the tail led to $Fe_2 > f_2$, and $Fe_1 = f_1$, driving the tail to move towards the light (Supplementary Fig. 34a). Typically, the sheet at α = 90° could crawl phototropically at a speed of ~0.04 mm s^{-1} (Supplementary Fig. 34b, c). Besides, at 0° < α < 90°, the gel rotated anticlockwise while crawling, and crawled clockwise at 90° < α < 180° (Supplementary Fig. 35). For example, at α = 45°, a counterclockwise crawling was delivered with a displacement of 3 mm and motion angle of 17.5° over 60 s of cyclic scanning (Supplementary Fig. 35b). Additionally, the gel at α = 90° could rotate clockwise by 360° under 100 cycles of the diagonal scanning from the upper left (Supplementary Fig. 36 and Supplementary Movie 5). For clear demonstration, different locomotion modes in different solvents were summarized (Fig. 4i and Supplementary Fig. 37). Even in the paraffin with high viscosity, the controllable movements at a displacement velocity of 0.024 mm s^{-1} and a rotating velocity of 1.75° s^{-1} were achieved for the crawling and rotation, respectively. Thus, the fabricated hydrogel robots implemented multi-gait locomotion whose amplitude and directionality were accurately regulated by the intrinsic structure. As for both the crawling and rotation motions, their driving force that determined the motion trajectory was the contraction force perpendicular to the lamellar structure. By decomposing the contraction force along the light scanning direction, the component of force in the parallel direction contributed to the displacement, while the vertical direction created torque to change the motion direction.

Controllable 3D self-propulsion locomotion in polar solvents

Besides programmable crawling and rotating motions in water and non-polar solvents, the ASPC hydrogel that reached the solvent exchange equilibrium in polar organic solvents could perform a manageable 3D self-propulsion locomotion under the stimulation of NIR light (Fig. 5a, Supplementary Fig. 38 and Supplementary Movie 6). Typically, when illuminated in ethanol, the gel spontaneously assumed an optimal posture for floating with low resistance under the asymmetry of temperature and flow fields induced by the photothermal effect (Supplementary Fig. 39a). With quickly repelling the ethanol through the unimpeded cell network, the robot rapidly floated up to the liquid-air interface with a depth of 50 mm within 3 s of illumination (Fig. 5b and Supplementary Fig. 39b). After reaching the interface, it could float stably on the liquid surface for several seconds under the action of surface tension. To examine the floating mechanism, multiphysics model based on the finite-element method (FEM) was employed to calculate the flow velocity and temperature distribution at different times (Supplementary Fig. 40 and Supplementary Note 1). The irradiated surface of the gel was regarded as a heat source, from which heat was transmitted to the fluid, forming a temperature gradient along the illumination direction. With increasing temperature under the continual irradiation, the upward liquid produced a buoyant flow[40]. It was simulated that the maximum buoyancy velocity reached 21.7 mm s^{-1} at 1.6 s when the temperature difference was set to be 10 K (Fig. 5b). Upon increasing the temperature gradient, the velocity of the induced convection was greatly improved (Supplementary Fig. 40c, d). The experimental results validated that the time of the hydrogel floating to a height of 30 mm decreased from 3.1 s to 1.1 s as the power intensity increased from 1.5 to 2.5 W cm^{-2} (Supplementary Fig. 41a). Furthermore, no obvious fatigue was recorded after floating for 100 cycles, indicating its excellent stability (Supplementary Fig. 41b). Notably, the gel achieved a maximum floating height of 400 mm at a floating speed of 13.2 mm s^{-1} (Supplementary Fig. 42a), outperforming the previously-reported soft floating robots (Supplementary Fig. 42b).

After arrival at the liquid-air interface, the continued illumination raised the local temperature and decreased the surface tension of the liquid around the gel correspondingly. A partial surface tension gradient was therefore produced, along which an impetus was generated to propel the hydrogel swimming navigation on the solvent surface under the Marangoni effect. The temperature and swimming velocity were monitored by changing the power intensity (Supplementary Fig. 43a). When the light power increased from 1.5 to 2.5 W cm^{-2}, the surface tension of the liquid surrounding the gel was decreased with the temperature of the gel increased, leading to an increased surface tension gradient in the solution and an enhanced Marangoni effect. The swimming velocity was therefore improved. Moreover, when decreasing surface tension of the solution, for example, decreasing the volume fraction of ethanol, the swimming velocity would decrease resulting from the weakened Marangoni effect (Supplementary Fig. 43b). These results indicated a swimming propulsion of the photothermal Marangoni effect. Noted that the navigation direction could be precisely controlled by the α of the gel rather than a complex shape design. At α = 0°, the hydrogel performed linear swimming along the direction of Marangoni propulsion (Fig. 5c, Supplementary Fig. 44 and Supplementary Movie 7). When changing the α, the locomotion mode transformed accordingly. This was because when the gel was heated, the contraction force F_S was generated by the shrinkage of the polymer network, causing the gel to deviate from the direction of the Marangoni propulsion. The resultant force F, originated from the Marangoni propulsive force F_M and reacting force of contraction force F_S', generated a rotational torque τ_s, resulting in a rotational motion of gel around the centroid under the balance of buoyancy and gravity (Supplementary Fig. 45). The clockwise and anticlockwise rotational swimming were attained by regulating the α. Specifically, when α = 45°, the swimmer rotated clockwise at an angular velocity of $\omega = 1.57$ rad s^{-1} and took on anticlockwise rotation at $\omega = 1.05$ rad s^{-1} at α = 135° (Fig. 5d and Supplementary Movie 8). The time-dependent angular displacement θ was conformed to a sinusoidal curve (Fig. 5e). It was observed that the swimmer could rotate steadily for 845 s upon continuous irradiation (Supplementary Fig. 46). Furthermore, the floating-swimming movements worked smoothly under NIR stimulation in

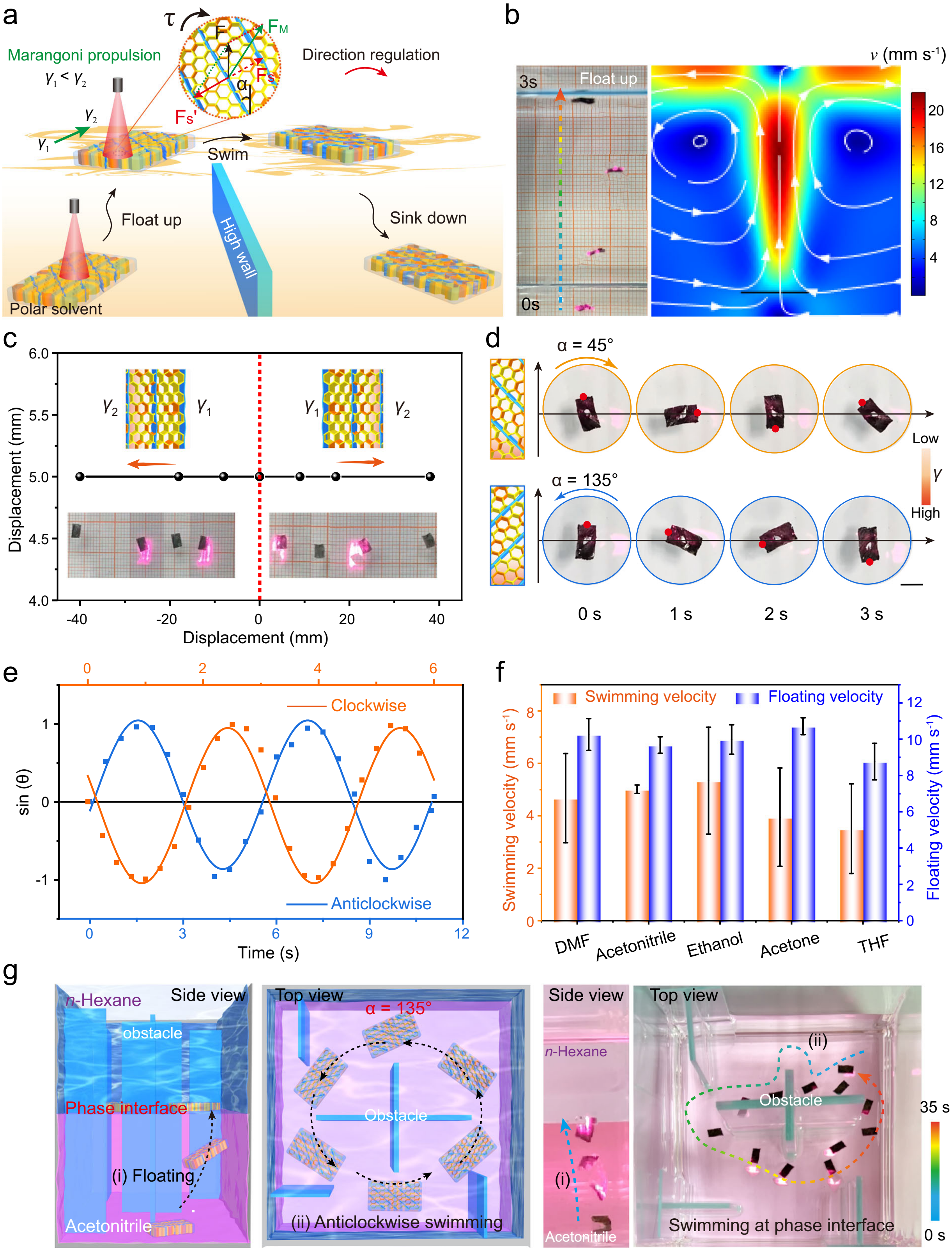

other polar solvents with the density less than water including DMF, acetonitrile, acetone and THF (Fig. 5f).

To this end, the 3D self-propulsion motion with the controllable directionality on the liquid surface was easily actualized by taking advantage of high structural anisotropy. This was different from the traditional Marangoni swimmers[41,42]. Traditionally, because of unsatisfactory heat transfer efficiency during convection, the floating height was limited. Furthermore, to control the swimming trajectory, it was necessary to selectively focus light on different regions of the absorber to affect the direction of the applied force or provide a specific direction of light-absorbing materials within the device[43,44]. This greatly reduced the programmability and efficiency of motion, making it impossible to satisfy the requirements of multifunctional soft robots. In sharp contrast, the ASPC robot demonstrated potentials

Fig. 5 | Controllable 3D self-propulsion locomotion in polar solvents. **a** Schematic diagram demonstrated the hydrogel performing 3D self-propulsion motion driven by NIR light to pass through an obstacle. Initially, the buoyancy flow stimulated the gel to perform a 3D drifting motion under the photothermal effect. Then, programmable swimming in the liquid surface was driven by the Marangoni effect. When the light irradiated at one end of the gel, the temperature increase caused the surface tension $\gamma_1 < \gamma_2$, and Marangoni propulsion force F_M was along the surface tension gradient. Meanwhile, the contraction force F_S in the irradiated region perpendicular to the lamellae produced a reaction force F_S' exerted by the liquid. A torque τ_s generated by the resultant force of the F_M and F_S' drove a rotational swimming. **b** Optical images and simulation of convective velocity distribution around the gel during the floating. A maximum flow velocity was 21.7 mm s^{-1} at 1.6 s when the initial temperature difference was 10 K. **c** Schematic illustration and superimposed photographs showed linear swimming of the hydrogel at α = 0°. The red arrows indicated the swimming directions. **d** Sequencing images showed the clockwise or anticlockwise rotational swimming of the hydrogels at α = 45° or 135° within 3 s of radiation. One end of the gel marked by red dot indicated the angular displacements of the rotation. **e** Sine of angular displacement (sinθ) as a function of time and sine curve fitting showed steady rotation under the light. **f** Summary of the floating and linear swimming speeds in different polar solvents. Data are presented as mean values ± SD ($n = 3$). **g** Schematic diagrams and optical images of the hydrogel at α = 135° performing 3D self-propulsion under NIR stimulation to cross the obstacles at the interface of acetonitrile and *n*-hexane.

to navigate across unstructured environments including the interface of different solvents without complex accessories (Fig. 5g). It was observed that the robot at α = 135° reached the interface of *n*-hexane and acetonitrile through floating motion induced by NIR light, and then crossed the set maze through changing the swimming mode of anticlockwise rotation under the synergy of the Marangoni effect and structure-guided shrinkage (Supplementary Movie 9).

Discussion

In conclusion, we reported a strategy of confined assembly polymerization of oriented porous channels into a highly ordered nanoassembly framework to fabricate environmentally tolerant and multi-stimuli responsive ASPC hydrogels with hierarchically anisotropic cellular structure by programmable directional freezing assisted two-stage in situ polymerization. Benefitting from highly anisotropic layered scaffold structure and low-tortuous open mass transfer channels, the ASPC hydrogel exhibited ultrafast anisotropic deformation under the stimulation of heat, light and solvent. With the help of the reinforced-concrete components and robust structure, the gel could stably adapt in all-polarity solvent environments with highly consistent responsive capability after 100 days of aging. These prominent performances enabled the gels to perform photoactivated programmable locomotion in various solvents that encoded in their internal anisotropic structures, including steered crawling in water and non-polar solvents, and controllable 3D self-propulsion swimming motion in polar solvents. The design concept and fabrication method in this work will open an effective avenue to access rapid responsive and stable hydrogel materials with controllable movements in complex solvents by regulating hierarchy and precision of assembly structure, and may broaden the application scope of flexible intelligent actuators in unusual harsh environments.

Methods

Fabrication of ASPC hydrogel

Firstly, a self-made bidirectional freezing device was built for the assembly of the lamellar architecture, which was made of a foam box containing liquid nitrogen, a steel plate with high thermal conductivity and a silicone mold with adjustable shape. The mixture consisting of AgNW suspension (25 mg mL^{-1}) and SA solution (20 mg mL^{-1}) was dropped onto a silicone mold placing in a specific position that was 1 cm away from the cold source on the steel plate. Then, liquid nitrogen was continuously and slowly added to maintain the desired height during the freezing process. After completely frozen in 30 min, the sample was freeze dried using a Labconco FreeZone freeze-dryer (pressure: 10 Pa, temperature: −56 °C) for 48 h. To enhance the robustness of the scaffold, the obtained ASAA network was further ionically crosslinked by immersing in ethanol solution of $CaCl_2$ (20 mg mL^{-1}) for 10 min followed by solvent exchange with deionized water.

In the following, the predesigned ASAA matrix was immersed in 5 mL solution (viscosity: 3.37 mPa s) containing 1 g of NIPAM as monomer, 2 mg of MBAA as crosslinker, 25 mg of $K_2S_2O_8$ as initiator and 800 μL of CNTs (2 wt%) for 1 min. To ensure full filling of the scaffold with the precursors, the vacuum dryer (pressure: −0.1 MPa) was applied to continuously press the PNIPAM solution into the ASAA scaffold until no obvious bubbles emerged from the scaffold (1 min). Noted that to prevent the precursor solution from polymerizing before freezing assembly, the above mixture was placed in an ice bath which was controlled at ~5 °C in the filling process. By quickly adding 20 μL of TEMED as accelerator, the polymerizable mixture was transferred to a cold plate at −30 °C and unidirectionally frozen in the direction parallel to the ASAA lamella for 5 min. Following with the cryopolymerization in the refrigerator (−18 °C) for 18 h and room temperature polymerization for 5 h, the ASPC hydrogel was finally fabricated. Similarly, the A_{10}SAA and A_{45}SAA scaffolds were prepared by controlling the contents of AgNWs at 10 and 45 mg mL^{-1}, respectively. By directional freezing assisted polymerization of the NIPAM-CNT solution in the A_{10}SAA and A_{45}SAA scaffolds as that of ASPC, the A_{10}SPC and A_{45}SPC hydrogels were fabricated. Another comparative hydrogel was fabricated through in-situ polymerization of the PNIPAM-CNT network in the ASAA scaffold without the directional freezing assembly, defined as ASAA-PC hydrogel.

Materials characterization

Structural and compositional analyses of the samples were performed by SEM images and elemental mappings on a Zeiss Merlin Compact field-emission scanning electron microscope equipped with an Oxford Inca energy instrument at an acceleration voltage of 5 kV. Optical microscope image was measured on a microscope MV3000. The freeze-dried hydrogel embedding resin was used to obtain ultrathin slices parallel to the Ag/SA lamellae by Leica EM UC7 cryo microtome, and deposited on silicon wafer and copper mesh for subsequent observation. The morphology, microstructure and elemental mapping of the AgNW nanopillars were observed using EDS-SEM and HAADF-STEM (JEM1400FLASH). The internal morphology of the ASPC hydrogel was 3D visualized by X-ray computed microtomography (Xray-Zeiss-Xradia-520-Versa) operating at an accelerating voltage of 100 kV. Raman spectroscopy and spatial Raman mapping were recorded on a LabRAM-HR (Horiba JY) confocal laser micro-Raman spectrometer. The temperature change under NIR (808 nm) irradiation was monitored by a Fluke Ti400 infrared imager. The mechanical properties of ASPC hydrogels in the equilibrated state were measured at room temperature by using an Instron 5965 A testing instrument with the stretch speed of 100 mm min^{-1}. The stimuli-responsive deformation of the hydrogel was recorded by a camera and then analyzed by measuring the variations of gel dimensions. The relative dimensional change was calculated as L_t/L_0, where L_0 was initial dimension and L_t was the dimension after deformation. The swelling ratio was calculated as L_t/L_0. The deformation and recovery rates were calculated as $(L_0\text{-}L_t)/t$, where t was deformation or recovery time.

Data availability

The data supporting the findings of this study are included in the paper and its Supplementary Information. All data are available from the corresponding author on request. Source data are provided with this paper.

References

1. Nepal, D. et al. Hierarchically structured bioinspired nanocomposites. *Nat. Mater.* **22**, 18–35 (2023).
2. Dawson, C., Vincent, J. & Rocca, A.-M. How pine cones open. *Nature* **390**, 668 (1997).
3. Wu, S., Hong, Y., Zhao, Y., Yin, J. & Zhu, Y. Caterpillar-inspired soft crawling robot with distributed programmable thermal actuation. *Sci. Adv.* **9**, eadf8014 (2023).
4. Zhu, Q. L. et al. Animating hydrogel knotbots with topology-invoked self-regulation. *Nat. Commun.* **15**, 300 (2024).
5. Guo, K., Yang, X., Zhou, C. & Li, C. Self-regulated reversal deformation and locomotion of structurally homogenous hydrogels subjected to constant light illumination. *Nat. Commun.* **15**, 1694 (2024).
6. Zhou, Y. H. et al. A multimodal magnetoelastic artificial skin for underwater haptic sensing. *Sci. Adv.* **10**, eadj8567 (2024).
7. Zheng, Z. et al. Programmable aniso-electrodeposited modular hydrogel microrobots. *Sci. Adv.* **8**, eade6135 (2022).
8. Jiang, Z. & Song, P. Strong and fast hydrogel actuators. *Science* **376**, 245 (2022).
9. Du, X. et al. Fast transport and transformation of biomacromolecular substances via thermo-stimulated active "inhalation-exhalation" cycles of hierarchically structured smart PNIPAM-DNA hydrogels. *Adv. Mater.* **35**, 2206302 (2023).
10. Chen, Z. et al. Paper-structure inspired multiresponsive hydrogels with solvent-induced reversible information recording, self-encryption, and multidecryption. *Adv. Funct. Mater.* **32**, 2201009 (2022).
11. Kamata, H., Akagi, Y., Kayasuga-Kariya, Y., Chung, U. I. & Sakai, T. "Nonswellable" hydrogel without mechanical hysteresis. *Science* **343**, 873–875 (2014).
12. Reed, R., Houston, T. W. & Todd, P. M. Structure and function of the sarcolemma of skeletal muscle. *Nature* **211**, 534–536 (1966).
13. Zhu, Q. L. et al. Light-steered locomotion of muscle-like hydrogel by self-coordinated shape change and friction modulation. *Nat. Commun.* **11**, 5166 (2020).
14. Zhu, Q. L. et al. Distributed electric field induces orientations of nanosheets to prepare hydrogels with elaborate ordered structures and programmed deformations. *Adv. Mater.* **32**, 2005567 (2020).
15. Li, M., Mei, J., Friend, J. & Bae, J. Acousto-photolithography for programmable shape deformation of composite hydrogel sheets. *Small* **18**, 2204288 (2022).
16. Nasseri, R. et al. Programmable nanocomposites of cellulose nanocrystals and zwitterionic hydrogels for soft robotics. *Nat. Commun.* **14**, 6108 (2023).
17. Chen, L. et al. Anisotropic thermoresponsive hydrogels by mechanical force orientation of clay nanosheets. *Polymer* **192**, 122309 (2020).
18. Li, C. et al. Fast and programmable locomotion of hydrogel-metal hybrids under light and magnetic fields. *Sci. Robot.* **5**, eabb9822 (2020).
19. Itahara, T., Tsuchida, T. & Morimoto, M. Solvent-driven swelling and shrinking of poly(NIPAM) gels crosslinked by tris-methacrylated phloroglucinol derivatives. *Polym. Chem.* **1**, 1062–1066 (2010).
20. Huang, J., Liao, J., Wang, T., Sun, W. & Tong, Z. Super strong dopamine hydrogels with shape memory and bioinspired actuating behaviours modulated by solvent exchange. *Soft Matter* **14**, 2500–2507 (2018).
21. Wei, S. et al. Bioinspired synergistic fluorescence-color-switchable polymeric hydrogel actuators. *Angew. Chem. Int. Ed.* **58**, 16243–16251 (2019).
22. Wang, Y. et al. Highly compressible and environmentally adaptive conductors with high-tortuosity interconnected cellular architecture. *Nat. Synth.* **1**, 975–986 (2022).
23. Cui, Y. et al. Smart sponge for fast liquid absorption and thermal responsive self-squeezing. *Adv. Mater.* **32**, 1908249 (2020).
24. Yan, Q. et al. Bio-inspired stimuli-responsive $Ti_3C_2T_x$/PNIPAM anisotropic hydrogels for high-performance actuators. *Adv. Funct. Mater.* **33**, 2301982 (2023).
25. Jian, Y. et al. Stimuli-responsive hydrogel sponge for ultrafast responsive actuator. *Supramol. Mater.* **1**, 100002 (2022).
26. Liu, J. et al. Two-step freezing polymerization method for efficient synthesis of high-performance stimuli-responsive hydrogels. *ACS Omega* **5**, 5921–5930 (2020).
27. Zhao, Y. et al. Somatosensory actuator based on stretchable conductive photothermally responsive hydrogel. *Sci. Robot.* **6**, eabd5483 (2021).
28. Zong, L. et al. Activation of actuating hydrogels with WS_2 nanosheets for biomimetic cellular structures and steerable prompt deformation. *ACS Appl. Mater. Interfaces* **9**, 32280–32289 (2017).
29. Zhao, H. et al. Cloning nacre's 3D interlocking skeleton in engineering composites to achieve exceptional mechanical properties. *Adv. Mater.* **28**, 5099–5105 (2016).
30. Song, L. et al. Visualizing the toughening mechanism of nanofiller with 3D X-ray Nano-CT: Stress-induced phase separation of silica nanofiller and silicone polymer double networks. *Macromolecules* **50**, 7249–7257 (2017).
31. Wang, Y., Seebald, J. L., Szeto, D. P. & Irudayaraj, J. Biocompatibility and biodistribution of surface-enhanced Raman scattering nanoprobes in zebrafish embryos: In vivo and multiplex imaging. *ACS Nano* **4**, 4039–4053 (2010).
32. Bharadwaj, S. et al. Cononsolvency of thermoresponsive polymers: Where we are now and where we are going. *Soft Matter* **18**, 2884–2909 (2022).
33. Zhu, P. W. & Napper, D. H. Coil-to-globule type transitions and swelling of poly(N-isopropylacrylamide) and poly(acrylamide) at latex interfaces in alcohol–water mixtures. *J. Colloid Interface Sci.* **177**, 343–352 (1996).
34. Wang, F., Shi, Y., Luo, S., Chen, Y. & Zhao, J. Conformational transition of poly(N-isopropylacrylamide) single chains in its cononsolvency process: A study by fluorescence correlation spectroscopy and scaling analysis. *Macromolecules* **45**, 9196–9204 (2012).
35. Chen, L. et al. Multi-stimuli responsive, shape deformation, and synergetic biomimetic actuator. *Chem. Eng. J.* **480**, 148205 (2024).
36. Wei, X. et al. Remotely controlled light/electric/magnetic multiresponsive hydrogel for fast actuations. *ACS Appl. Mater. Interfaces* **15**, 10030–10043 (2023).
37. Shen, T. et al. Remotely triggered locomotion of hydrogel mag-bots in confined spaces. *Sci. Rep.* **7**, 16178 (2017).
38. Chang, D. P., Dolbow, J. E. & Zauscher, S. Switchable friction of stimulus-responsive hydrogels. *Langmuir* **23**, 250–257 (2007).
39. Vernerey, F. & Shen, T. The mechanics of hydrogel crawlers in confined environment. *J. R. Soc. Interface* **14**, 20170242 (2017).
40. Hou, G. et al. Self-regulated underwater phototaxis of a photoresponsive hydrogel-based phototactic vehicle. *Nat. Nanotechnol.* **19**, 77–84 (2024).
41. Wang, W. et al. Direct laser writing of superhydrophobic PDMS elastomers for controllable manipulation via marangoni effect. *Adv. Funct. Mater.* **27**, 1702946 (2017).
42. Hou, K. et al. Programmable light-driven swimming actuators via wavelength signal switching. *Sci. Adv.* **7**, eabh3051 (2021).
43. Wang, W. et al. Laser-induced graphene tapes as origami and stick-on labels for photothermal manipulation via marangoni effect. *Adv. Funct. Mater.* **31**, 2006179 (2020).

44. Okawa, D., Pastine, S. J., Zettl, A. & Fréchet, J. M. Surface tension mediated conversion of light to work. *J. Am. Chem. Soc.* **131**, 5396–5398 (2009).
45. Pi, M. et al. Rapid gelation of tough and anti-swelling hydrogels under mild conditions for underwater communication. *Adv. Funct. Mater.* **33**, 2210188 (2022).
46. Ren, J. et al. An anti-swellable hydrogel strain sensor for underwater motion detection. *Adv. Funct. Mater.* **32**, 2107404 (2021).
47. Li, F. et al. Bioinspired nonswellable ultrastrong nanocomposite hydrogels with long-term underwater superoleophobic behavior. *Chem. Eng. J.* **375**, 122047 (2019).
48. Dou, X. et al. One-step soaking strategy toward anti-swelling hydrogels with a stiff "armor". *Adv. Sci.* **10**, 2206242 (2023).
49. He, S. et al. Non-swelling and anti-fouling MXene nanocomposite hydrogels for underwater strain sensing. *Adv. Mater. Technol.* **7**, 2101343 (2021).
50. Fan, H., Wang, J. & Jin, Z. Tough, swelling-resistant, self-healing, and adhesive dual-cross-linked hydrogels based on polymer–tannic acid multiple hydrogen bonds. *Macromolecules* **51**, 1696–1705 (2018).
51. Xu, P. et al. A nonswellable gradient hydrogel with tunable mechanical properties. *J. Mater. Chem. B* **8**, 2702–2708 (2020).

Acknowledgements

This work is supported by the National Natural Science Foundation of China (22471052, 22171066, 21922104 (H.P.C.), and 22293044 (S.H.Y).), the National Key Research and Development Program of China (2021YFA0715700 and 2018YFE0202201 (S.H.Y.)) and the Fundamental Research Funds for the Central Universities (JZ2023YQTD0074 (H.P.C.), and JZ2021HGPA0064 (H.Q.)).

Author contributions

H.P.C. and S.H.Y. supervised the project, conceived the idea and designed the experiments. X.Y. planned and performed the experiments, collected and analyzed the data. H.C. and H.Q. contributed to the structural analyses. Q.H.W. helped with the materials synthesis. X.Y., H.P.C. and S.H.Y. wrote the paper, and all authors discussed the results and commented on the manuscript.

Competing interests

The authors declare no competing interests.

Additional information

Supplementary information The online version contains supplementary material available at https://doi.org/10.1038/s41467-024-53549-y.

Correspondence and requests for materials should be addressed to Huai-Ping Cong or Shu-Hong Yu.

Peer review information *Nature Communications* thanks Junjie Yang and the other, anonymous, reviewers for their contribution to the peer review of this work. A peer review file is available.

Reprints and permissions information is available at http://www.nature.com/reprints